

Multiple cracking analysis of HTPP-ECC by digital image correlation method

Burak Felekoğlu^{*1} and Muhammer Keskinates^{2a}

¹Department of Civil Engineering, Dokuz Eylül University, Tinaztepe, Buca, 35397, İzmir / Turkey

²The Graduate School of Natural and Applied Sciences, Dokuz Eylül University, İzmir / Turkey

(Received March 9, 2015, Revised December 17, 2015, Accepted March 3, 2016)

Abstract. This study aims to characterize the multiple cracking behavior of HTPP-ECC (High tenacity polypropylene fiber reinforced engineered cementitious composites) by Digital Image Correlation (DIC) Method. Digital images have been captured from a dogbone shaped HTPP-ECC specimen exhibiting 3.1% tensile ductility under loading. Images analyzed by VIC-2D software and ε_{xx} strain maps have been obtained. Crack widths were computed from the ε_{xx} strain maps and crack width distributions were determined throughout the specimen. The strain values from real LVDTs were also compared with virtual LVDTs digitally attached on digital images. Results confirmed that it is possible to accurately monitor the initiation and propagation of any single crack or multiple cracks by DIC at the whole interval of testing. Although the analysis require some post-processing operations, DIC based crack analysis methodology can be used as a promising and versatile tool for quality control of HTPP-ECC and other strain hardening composites.

Keywords: fiber reinforced composite; multiple cracking; high tenacity polypropylene fiber; tensile test; digital image correlation

1. Introduction

Engineered cementitious composites (ECC) are a family of engineered high performance fiber reinforced cementitious composites and have been developed to address the brittleness shortcomings of conventional fiber reinforced concrete and plain concrete. ECC has tensile ductility as much as three hundred times that of normal concrete. For this reason, it is also a member of strain hardening cementitious composites (or SHCC). ECC derives its tensile ductility by deliberately allowing cracks to grow out from pre-existing flaws in a controlled manner (Li, 2012). Typically, the damage pattern under uniaxial tension presents a large number of closely spaced micro-cracks, spaced a few millimeters apart (multiple cracking). In this manner, localized catastrophic brittle fracture is suppressed. The ductility of ECC is the sum total of distributed deformation resulting from the diffused micro-crack damage. Two complimentary criteria

*Corresponding author, Associate Professor, E-mail: burak.felegoglu@deu.edu.tr

^aPh.D. Student, E-mail: muhammer.keskinates@deu.edu.tr

(strength criterion and the energy criterion) based on micromechanical model proposed by Li *et al.* (2001) should be provided in order to attain the multiple cracking response. Micro-mechanics based model serves as a rational methodology for developing cementitious composites with high tensile ductility combined with special attributes or functions. Micromechanics based model links microscale constituent parameters to fiber bridging constitutive behavior in the mesoscale. Steady state crack analysis connects fiber bridging property of composite to its tensile strain hardening capacity at macroscale. The stress-crack opening relationship ($\sigma(\delta)$) as the constitutive law of fiber bridging behavior can be derived by using analytic tools of fracture mechanics, micromechanics, and probabilistic. In particular, the energetics of tunnel crack propagation along fiber/matrix is used to quantify the debonding process and the bridging force of a fiber with given embedment length (Lin *et al.* 1999). Probabilistics is introduced to describe the randomness of fiber location and orientation with respect to a crack plane. The random orientation of fiber also necessitates the accounting of the mechanics of interaction between an inclined fiber and the matrix crack. As a result, the $\sigma(\delta)$ curve is expressible as a function of micromechanics parameters (Yang 2007). Details of the model can be found in Li *et al.* (2001).

In most cases steel or synthetic fibers have been employed as fiber reinforcement for cement-based composites. Among synthetic fibers, high tenacity PVA fibers have been preferred on large scale and industrial bases, considering its intrinsic properties: high tensile strength, high modulus, and low elongation, high durability in alkaline matrix, hydrophilic behavior, good dispersion in water, and good bonding with cement paste (Ikai *et al.* 2006). From the view point of micromechanical theory of ECC, an optimized chemical bond between PVA fibers and cementitious matrix is required for ECC with saturated multiple cracking. PVA fibers pre-processed with oiling agent well suited with this requirement and employed in many ECCs (Li *et al.* 2001). However, the high cost of PVA and worldwide availability problems limits its usage in ECC design. Polypropylene (PP) resin is a promising alternative to produce fibers suitable for ECC design as a relatively less expensive and easily accessible raw material. For this purpose, high tenacity polypropylene (HTPP) fibers, with improved frictional interface and affinity to Portland cement matrix have been developed in recent years (Ikai *et al.* 2006). These fibers were also successfully used in ECC design (Felekoğlu *et al.* 2014).

The ductility of ECC as a result of its multiple cracking potential can only be verified by real time capturing and analyzing the damage pattern under uniaxial tension. It is not easy or sometimes impossible to accurately monitor the width change of closely spaced micro-cracks with conventional displacement measurement methods (point-wise sensors (PWSs) such as linear potentiometers, crack opening gauges, and strain gauges) and/or imaging techniques throughout the whole testing interval. Since many microcracks can be randomly formed throughout the specimen surface, a full-field strain mapping method with micrometer scale resolution is mandatory for this purpose. 2D-DIC method (as a non-contact optical measurement technique) is an appropriate solution to detect in plane displacements and to calculate local strains at the whole surface of specimen. The method suggested a comparison of the digital images for various small regions (known as subsets) throughout the images before and after deformation, locating the positions of each of these subsets after deformation through digital image analysis (Sutton *et al.* 1983).

Sutton *et al.* (1983) and Chu *et al.* (1985) developed numerical algorithms and performed preliminary experiments using optically recorded images to show that the 2D-DIC approach can be applied to quantify rotations and deformations in solids. With the growth of worldwide interest, new DIC procedures are validated, modified, improved and numerical algorithms refined (Cofaru

et al. 2010, Passieux and Perie 2012, Chakinala 2013). Recent applications of DIC focused on measuring out of plane deformation with three dimensional (3D-DIC) and volumetric (V-DIC) correlation methods (Sutton *et al.* 2008, Malesa *et al.* 2013). DIC is being utilized to understand material deformation behavior in many experimental engineering applications including metal alloys (Canadinc *et al.* 2008, Efstathiou and Sehitoglu 2010, Dilibal 2013), polymers (Tao and Zia 2005, Jerabek *et al.* 2010), soft woods (Hild *et al.* 2002, Bergonnier *et al.* 2005), synthetic foams (Wang and Cuitino 2002), ceramics (Leplay *et al.* 2010), composites (Godara and Raabe 2007, Willems *et al.* 2009, Canal *et al.* 2012, Kashfuddoja 2014) and concrete (Caduff and Van Mier 2010, Shah and Kishen 2011, Shih and Sung 2013, Gencturk *et al.* 2014, Aggelis *et al.* 2016). More details regarding the basics of DIC approach can be found in a comprehensive book by Sutton *et al.* (2009).

2D-DIC serves as a versatile and valuable tool to monitor crack growth, stress intensity factor estimation and local crack tip zone measurement in experimental fracture mechanics applications (Abanto-Bueno and Lambros 2002, Hild and Roux 2006, Roux *et al.* 2009, Wu *et al.* 2011, Dehnavi *et al.* 2014). The feasibility of applying DIC technique to monitor pipeline cracks was tested and confirmed by Tung and Sui (2010). Furthermore, the crack development in a masonry wall and the effect of crack formation on seismic resistance of masonry structures was successfully examined with DIC (Tung *et al.* 2008). The validity of applying DIC technique in crack observation for non-homogeneous materials at different scales was also confirmed by recent studies (Liu *et al.* 2014, Ghorbani *et al.* 2015). DIC methods were recently used by Ohno and Li (2014) in order to determine the crack width distribution of a special type of composites prepared with no cement (PVA-EGC: fiber reinforced engineered geopolymer composites). Analysis results confirmed that saturated multiple cracking can be monitored by DIC and average crack widths were stabilized at about 40-50 μm between 1% to 4.5% tensile strain (Ohno and Li 2014).

In previous studies, DIC method has usually been employed to study the crack propagation of brittle materials or fiber reinforced composites exhibiting tensile softening behavior. Only a few studies dealt with the application of DIC method to characterize the multiple cracking potential of strain hardening composites (Ohno and Li 2014). The applicability of DIC method for monitoring the multiple crack development of HTPP-ECC has been investigated within the scope of this experimental study. Multiple cracking response and crack width distribution with increasing tensile strain has been analyzed by the proposed methodology based on DIC. The crack maps and histograms of composites at any stage of loading were also determined which can not be possible with the conventional methods of strain measurement. While DIC method allows the quantification of local strains throughout the whole surface of specimen, only the length change between two definite points can be measured by conventional methods. Experimental studies indicated that it is possible to correlate the cracks with local strain variations determined by DIC method. Furthermore, existence of any in plane alignment deviation of specimen from uniaxial tensile loading can be detected with the application of proposed DIC methodology.

2. Experimental studies

2.1 Mixture proportions and specimen preparation

The mixture proportion of HTPP-ECC specimen adapted from Yang (2007) is presented in Table 1. All powder ingredients were premixed in a Hobart mixer for 2 min. Water and HRWRA

Table 1 Mixture proportions of HTPP-ECC

Cement* (kg/m ³)	Fly ash** (kg/m ³)	Water (kg/m ³)	HRWR*** (kg/m ³)	HTPP fiber**** (kg/m ³)
412	1150	362	7.4	18

* Ordinary Portland cement (OPC) conforming the requirements of ASTM C150 Type I.

** ASTM C618 class F fly ash mainly composed of SiO₂ (44%), Al₂O₃ (23%), Fe₂O₃ (8%), and CaO (14%), with other compounds in trace amounts. 83% by weight is finer than 44 µm

*** A polycarboxylate-based high range water reducing (HRWR) admixture was used to achieve flowability.

****HTPP fiber diameter: 12 µm, length: 10 mm, density: 0.91 g/cm³, nominal tensile strength: 850 MPa, Young's modulus: 6 GPa, elongation at rupture: 21%.

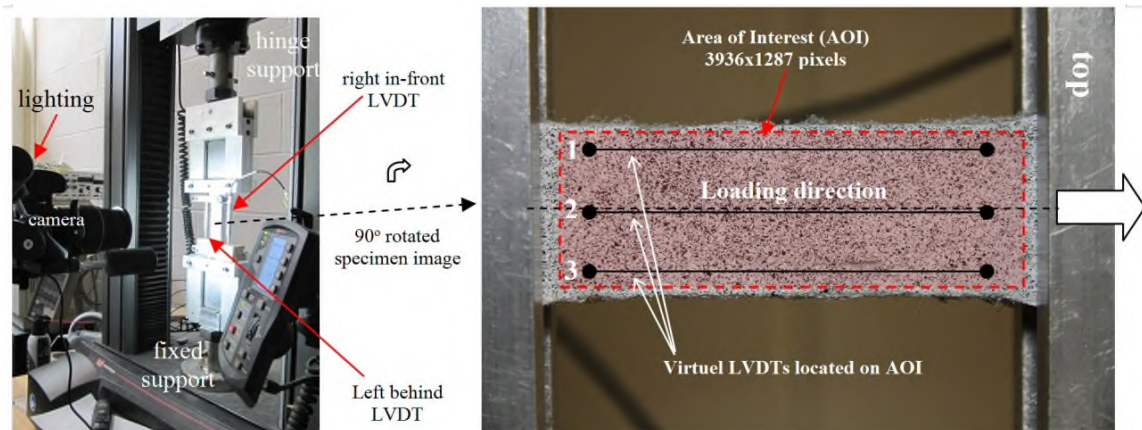


Fig. 1 Tensile testing setup with camera and lighting attachments (left). Magnified view of random speckle pattern applied on dogbone shaped specimen showing AOI (84.3x27.6 mm) (right)

were then added. All ingredients were mixed for 1 min at low speed and for 2 min at high speed, respectively. At the end of mixing procedure (prior to fiber addition) a highly flowable matrix with Marsh cone flow time of 23 s was obtained. HTPP fibers were finally added to the mixture and mixing prolonged for 3 min at high speed. Fresh material was poured into a dogbone shaped tensile test specimen mold conforming JSCE (2008) recommendations for standardized testing of HPRCCs and compacted with moderate vibration. HTPP-ECC specimen demolded one day after casting and cured in water (23±3°C) for 7 days and then stored at laboratory conditions (23±3°C, 45±5% RH) for 6 months. A random black and white speckle pattern was applied to the front face of the specimen prior to testing using mat spray paint (Fig. 1, right).

2.2 Tensile test setup

Tensile testing was conducted following the test method recommended by JSCE (2008). The dogbone specimens were gripped through wedge action on its slanting edges by using chucks on both ends. This chucking mechanism configuration with a fixed support at the bottom and a hinge support at the top of loading frame provides sufficient degrees of freedom in the grips to ensure the application of almost pure uni-axial tension force along the longitudinal loading axis (Fig. 1, left).

Uniaxial tension loading was performed at 0.5 mm/min. using a displacement controlled test system with maximum load capacity of 50 kN (Instron 5969). Tensile strain was computed from the average of extensions from two LVDTs attached on specimen (right in front and left back side of the specimen (Fig. 1, left)) divided by the gage length (100 mm).

2.3 Digital image correlation methodology

DIC methodology applied in this study can be divided into three parts: 1) pre-processing stage where digital images were collected, 2) image correlation analysis with software and 3) finally post-processing stage of crack detection and crack width analysis. Details are presented in the next paragraphs.

A CMOS camera with 8-bit intensity and 5184 by 3456 square pixel camera resolution was mounted on a tripod to capture digital images from specimen surface under tensile loading (Fig. 1). An artificial day-light source was also mounted to the camera in order to improve the gray scale intensity of captured images. Random speckle pattern previously applied on specimen's surface with high contrast permits the software to be able to identify and calculate the displacements with accuracy. The success of random speckle pattern is hidden in its high information content. The determination of motion vectors is only possible if the surface texture is non periodic without any preferred orientation. Repeating textures or using single pixels may lead to misregistration problems (Sutton *et al.* 2009). Random speckle patterns previously applied to the surface of specimen (as paint) adheres to surface and deform together with the surface, therefore correlation loss is minimized under large deformations. The speckle pattern provides the measurement of motion throughout the entire surface and it permits the use of a small section of speckles for pattern matching which is referred as a subset.

Digital raw images were automatically recorded with 5 s interval at the stage of loading. A total of 134 images have been captured at the end of test. Speckle surface texture change between the reference image (undeformed) and each deformed image was determined by using commercial 2-D image correlation analysis software Vic2D from Correlated Solutions (Cintron and Sauma, 2008). An area of interest (AOI) region was selected to monitor the in-plane deformations and local strains on specimen's surface (Fig. 1, right). The larger the size of this region, the more processing time will be needed for analysis. Since uniaxial tensile testing configuration used in this study provides pure tension loading, out-of-plane displacements is assumed to be sufficiently small and 2-D DIC is found adequate for analysis (Ohno and Li 2014).

The basic principle of DIC is to track the same pixel points located in various images. As discussed in previous paragraphs, it is not possible to track a single pixel in the deformed image, however a square collection of random gray scale pixels (called as subset) centered at the considered point can be tracked in the deformed images by using iterative digital image correlation algorithms. Various image matching algorithms can be used evaluate the similarity between the reference subset and its target one in the deformed image. These algorithms are expected to provide maximum possible image correlation (Cofaru *et al.* 2010, Pan *et al.* 2012). Different approaches of optimization criteria in the selection of appropriate matching algorithm can be listed as; squared sum of differences (SSD), normalized cross-correlation (NCC), zero-mean sum of squared differences (ZSSD), normalized sum of squared differences (NSSD), zero-mean normalized sum of squared difference (ZNSSD) and sum of absolute differences (SAD), respectively (Sutton *et al.* 2009).

The displacement field shows discontinuity at both sides of a crack, and hence the correlation

coefficient for the sub-images surrounding a crack is significantly reduced. The selection of subset size will affect the capability to resolve the strain variation. The strain close to the crack tip and specimen edge varies fast and can only be analyzed with small subset size, but once the sub-image is too small, the analysis accuracy of the displacement will be affected (Yaofeng and Pang 2007). Due to this reason, the appropriate subset size must be determined in accordance with the requirement of every analysis case. Furthermore, the spacing between each analyzed subsets at both x and y direction (called as step size) should be optimized in order to balance the strain map resolution (small step size is preferred for a high resolution of strain map) and computational effort (large step size is preferred for low computational effort) at the same time (Sutton *et al.* 2009). Subset size of 33×33 pixels and step size of 3 pixels were found suitable for this application based on preliminary investigations and previous DIC based crack analysis (Pan *et al.* 2008).

The 2D-DIC displacement data is converted into Lagrangian ϵ_{xx} strain values using method presented in Sutton *et al.* (2009). Since tensile cracking deals with differences in displacement values at x-direction, only ϵ_{xx} strain maps (strain parallel to loading direction) of loaded specimens were determined at the AOI. Vic2D software permits to locate virtual LVDTs at any location inside the AOI which is not possible with real LVDTs. In addition to real LVDTs, three virtual LVDTs have been located on AOI and strain values derived from these virtual LVDTs for comparison purpose (Fig. 1, right). Crack widths were computed from the ϵ_{xx} strain map by integrating strain with respect to length over the strain peak. Crack width distributions throughout the specimen and development of crack width histograms with increasing strain were also determined.

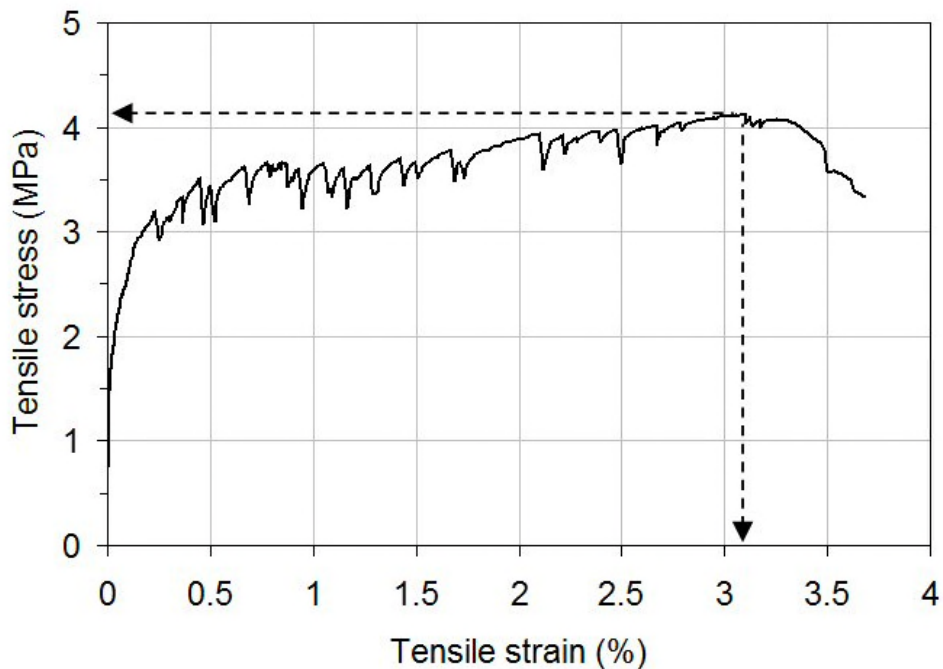


Fig. 2 Stress strain curve of HTPP-ECC specimen (dotted lines indicate tensile strength and ductility values)

3. Results and discussion

Tensile strength and ductility of HTPP-ECC specimen determined from stress-strain curve is 4.1 MPa and 3.1% respectively (Fig. 2). While the tensile strength of HTPP-ECC is comparatively similar to a high strength grade concrete (C60/70), its tensile ductility is nearly three hundred times higher than that of plain concrete or even conventional fiber reinforced concrete. ECC design requires steady state multiple cracking which can be provided by a combined optimization of fiber-matrix and interface properties. After the formation of first crack at 1.6 MPa (0.03% tensile strain), new cracks continued to form up to 3.1% tensile strain. At that while, many new cracks formed and stress level climbed up to 4.1 MPa. Once the fiber bridging capacity of any previously cracked section is exhausted, the crack responsible for the failure quickly widened. This type unstable crack widening failure usually observed in conventional fiber reinforced composites just after the first crack. The first crack will also be the failure crack of such composites which is not the case in HTPP-ECC as demonstrated in this study. Due to this reason conventional fiber reinforced composites exhibits much lower tensile ductility values compared to any type of ECC if designed and tested properly. The following sections deal with the results and discussion of applicability of DIC methods for strain and crack width analysis of HTPP-ECC.

3.1 Comparison of stress-strain curves obtained from real and virtual LVDTs

Stress-strain curves of HTPP-ECC specimen obtained from two real LVDTs and three virtual LVDTs located parallel to the loading axis have been presented in Fig. 3(a) and 3(b) respectively. These stress-strain curves were combined at the same graph with the time based intersection points. Note that each virtual LVDT strain value was determined from specimen photograph captured at 5 seconds interval. The stress and corresponding real LVDT strain values were matched with virtual LVDT strain values calculated by DIC method. As can be seen from Fig. 3(a), different tensile strain values were derived from separate LVDTs up to 0.7% depending on LVDT position. While the front right LVDT exhibited strain negative values (contraction), the left behind LVDT showed positive strain values (extension) (Fig. 1 and Fig. 3(a)). This situation indicates an initial slight in plane rotation of the specimen to the right side. After the formation initial microcracks, specimen deviated back and aligned again thanks to the fix-hinge joint tensile test configuration where the strain data from both LVDTs became similar above 0.7% tensile strain. In the case of virtual LVDTs, front surface of the specimen was focused and the stress-strain curves of three virtual LVDTs have been presented in Fig. 3(b). At low tensile strain values, virtual LVDTs generally overestimated the tensile strain values at any stress when compared to real LVDT results. It is important to note that strain curve derived from the front right real LVDT was more close to the third virtual LVDT curve which was located at the right side of specimen (Fig. 3(a)-3(b)). After 0.2% tensile strain value, formation of additional microcracks increased the tensile strain values measured by both real and virtual LVDTs in the same manner since specimen re-alignment provided again by fix-hinge tensile testing configuration (Fig. 3(c)). Relationship between strain values derived from real and virtual LVDTs has been presented in Fig. 4. According to Fig. 4, virtual LVDTs overestimated the strain values at low strain values. Detailed strain map analysis by DIC method (presented in the next section) showed that initial rotation of specimen was responsible for these higher strain values compared to real LVDTs. On the other hand, an underestimation of strain values compared to real LVDTs was observed at higher strain values near the specimen failure (indicated with a circle in Fig. 4). Based on the strain map

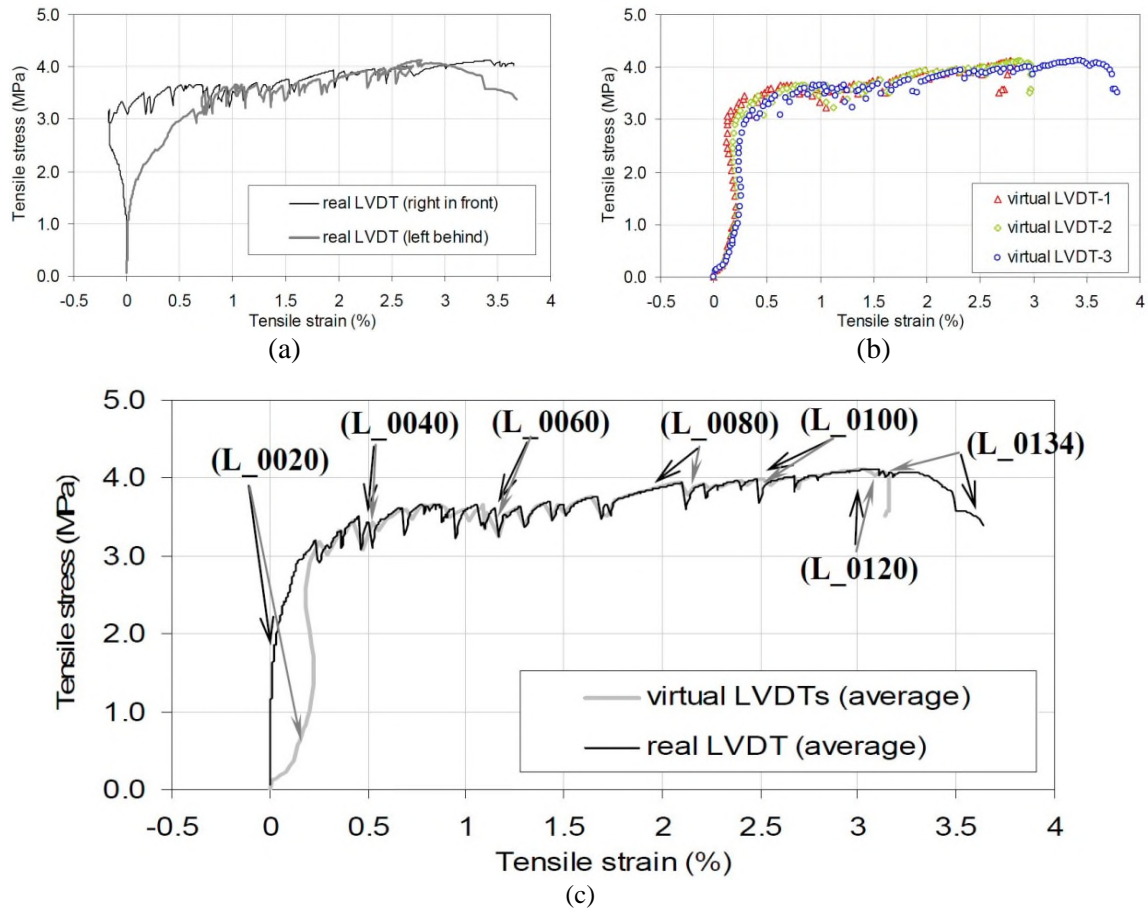


Fig. 3 Tensile stress-strain curves derived from individual real (a) and virtual (b) LVDTs, comparison of stress-average strain curves (c). (Arrows indicate the strain values of selected images for crack width analysis at corresponding instant strain values calculated from the length change data of real LVDTs).

analysis, the propagation of a crack formed out of AOI was found responsible for the observed difference between real and virtual LVDTs. These observations confirmed that virtual LVDTs are more sensitive to detect local surface strain variations at the initial and final periods of loading while real LVDTs are only capable of measuring the average displacement of the entire mass of specimen during testing. Any specimen rotation can be compensated by averaging the strain values obtained from real LVDTs located at both sides of the specimen.

3.2 ε_{xx} strain map monitoring, first crack detection

AOI of 134 images were analyzed with Vic2D and 11 representative strain maps have been presented in Fig. 5. At the beginning of loading, local ε_{xx} strain value at the whole map was zero. With the increase in tensile load, first crack visualized at the 20th image when the tensile stress was 1.85 MPa. Note that this value was very close to 1.60 MPa that was determined by real LVDTs from stress strain curve (Fig. 2). It is important to detect the first cracking strength of HTPP-ECC

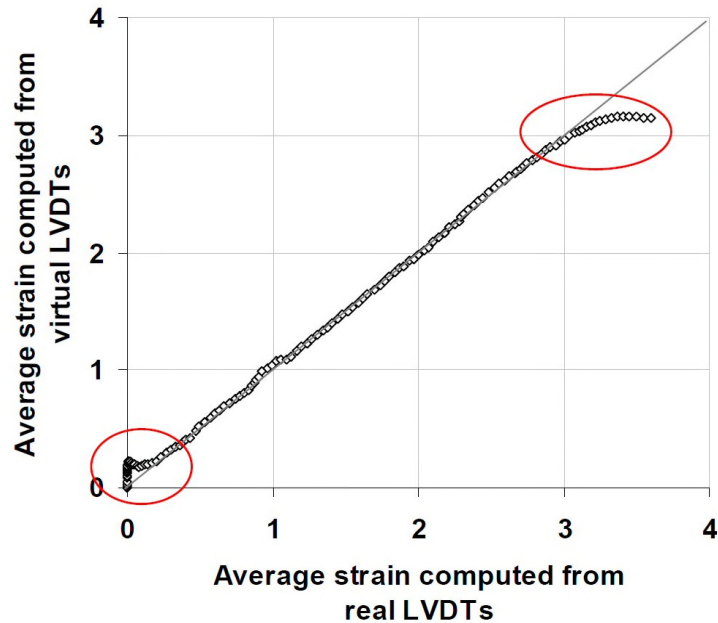


Fig. 4 Relationship between average strain values computed from real and virtual LVDTs

in order to check the strength criterion of ECC micromechanical design. The maximum flaw size and matrix fracture toughness determine the first cracking strength of ECC (Li *et al.* 2001). The ratio of fiber bridging strength (i.e. capacity of fibers at the weakest cracked section) to first cracking strength should be maximized in order to improve the robustness of saturated cracking (Li 2012).

New formed cracks and extension of previously formed cracks which indicates multiple cracking can be monitored from local ε_{xx} strain maps presented in Fig. 5. The color of cracked regions displayed significantly higher local strain values compared to regions with no cracking. Color difference was progressively increased with specimen elongation which can be attributed to crack widening (Fig. 5). Local strain maps also gave some valuable clues to interpret the possible causes of differences in real LVDT and virtual LVDT values at the initial and final moments of testing. As shown in Fig. 4, strain values derived from virtual LVDT was higher than values calculated from real LVDTs at the beginning of testing. Local ε_{xx} strain maps clearly showed that cracks started to form from the right side of the specimen (bottom side in Fig. 4 since the specimen was rotated 90° to the right) and due to this reason specimen bended left. At that moment, while one real LVDT (right front) started to display elongation, other one (left back) started to display closure which was previously confirmed by individual real LVDT measurement (Fig. 3(a)). These two observations confirmed that specimen bended left at the initial periods of testing. While the virtual LVDT value of image L_0020 captured at the 100th second of testing was 0.21%, average strain value of real LVDTs was only 0.03%. The initial settling of specimen heads to the chuck mechanism was possibly responsible for this initial bending effect. After the formation of a few initial cracks HTPP-ECC specimen started to re-align parallel to the loading axis thanks to its multiple cracking behavior. In most cases, conventional fiber reinforced composites with such a fiber dosage (2%) are not able to exhibit multiple cracking behavior. Due to this reason, specimens

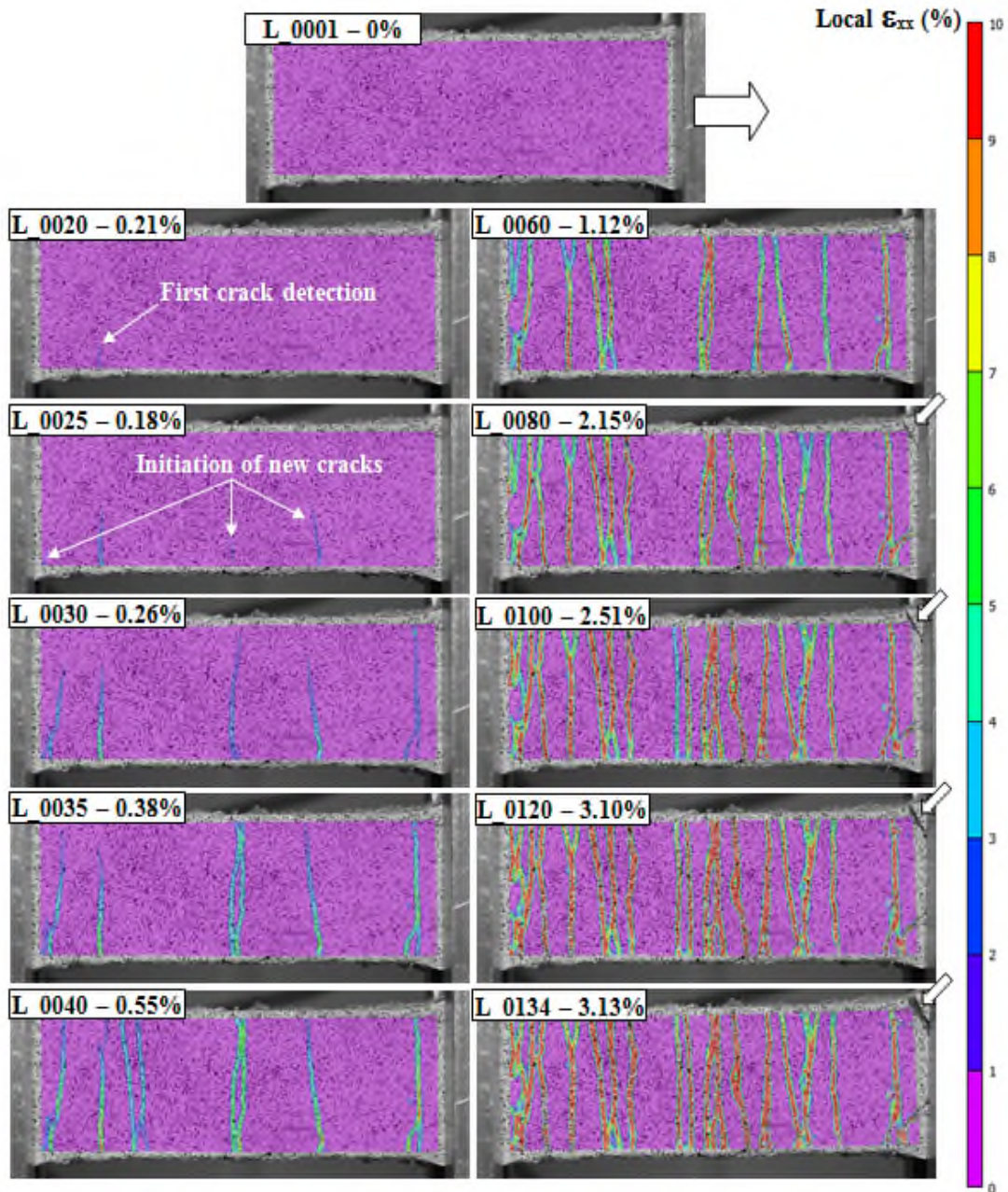


Fig. 5 Local ϵ_{xx} strain maps at 11 different elongations. (Boxes indicate: specimen code – average virtual LVDT strain)

of such composites can not re-orientation to the loading direction. The ability of HTPP-ECC specimen to deviate back to loading axis can be tracked from repeatedly converging real and

Table 2 Crack width analysis results of selected images and corresponding strain values.

Image code	Time of image capture (s)	Real LVDT strain (%)	Virtual LVDT strain (%)	Cumulative Crack number	Average crack width* from DIC (μm)
L_0001	0	0	0	--	--
L_0020	100	0.03	0.21	1	n.d.**
L_0025	125	0.10	0.18	4	n.d.**
L_0030	150	0.23	0.26	5	18 \pm 5
L_0035	175	0.38	0.38	6	25 \pm 5
L_0040	200	0.53	0.55	8	41 \pm 13
L_0060	300	1.11	1.12	10	80 \pm 13
L_0080	400	1.83	2.15	14	89 \pm 18
L_0100	500	2.47	2.51	18	99 \pm 26
L_0120	600	3.03	3.10	19	110 \pm 32
L_0134	675	3.67	3.13	19	115 \pm 29

* \pm 1 standard deviation

**Since cracks were not reached to the center line parallel to loading axis, crack widths were not detected.

virtual LVDT values presented in Table 2. After 150th second, nearly similar strain values were obtained both from real and virtual LVDTs which confirm the completion of specimen alignment parallel to loading. This situation was valid up to 600 s which corresponds to approximately 3%. After 3% strain, a crack formed out of AOI began to enlarge and part of this crack can be observed at the top right corner of images. This crack randomly formed out of AOI was the crack possessing the weakest fiber bridging capacity and rapidly widened after 3% strain (indicated by white arrows in Fig. 5). At that moment real LVDTs had the ability to measure this crack widening effect on strain (since this rapidly widening crack was inside the LVDT measuring range: 100 mm) However, virtual LVDTs can not detect this crack widening since AOI length is 84.3 mm. Due to this reason strain values derived from virtual LVDTs lagged behind real LVDTs. As seen in Table 2, while real LVDTs indicated a strain increment from 3.03% to 3.67% between 600th and 675th seconds of testing, strain values derived from virtual LVDTs were nearly the same (3.10% and 3.13% respectively).

It can be concluded that both real and virtual LVDTs present the same strain values between 0.2-3%. At lower strain values difference between real and virtual LVDTs arised from initial alignment attempts of specimen and at the end of testing crack widening out of AOI was responsible for the observed strain difference (Fig. 4). Detection of rapidly widening crack (failure crack) at the end of testing is extremely important to improve the multiple cracking capacity of ECCs. The fiber distribution at this section (local fiber dosage and orientation) determines the fiber bridging capacity of related section (Li 2001). Any problems with these parameters may reduce the multiple cracking performance of ECC. Fiber distribution analysis on this section may help the designer to improve the multiple cracking ability of ECC.

3.3 Crack number and crack width distribution analysis

As shown in previous section, cracked regions can be differentiated from uncracked ones with ϵ_{xx} local strain contour maps. It is possible to determine the local strain distribution on any line

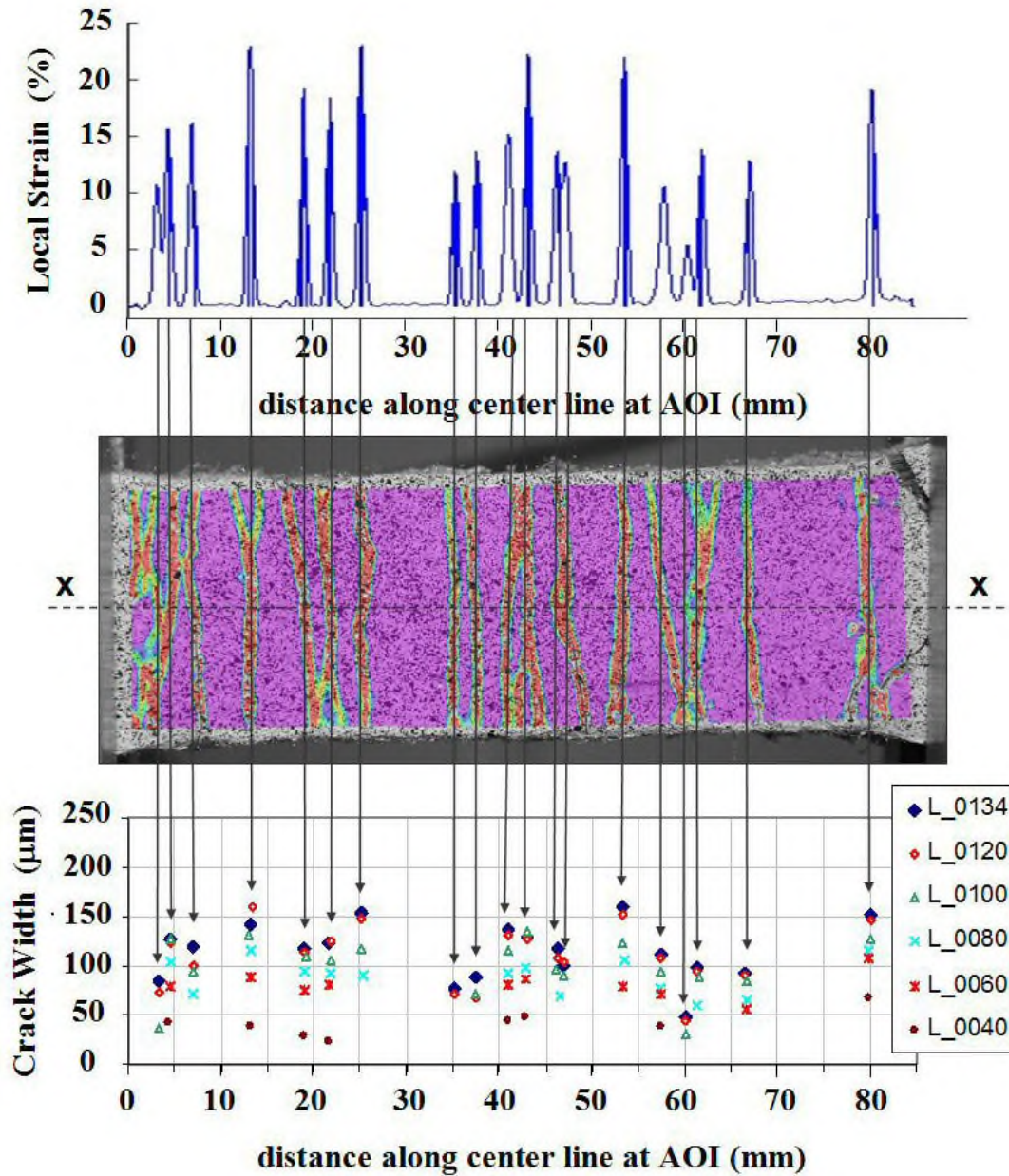


Fig. 6 Local strain distribution and corresponding strain map of image L_0134 (at 3.13% tensile strain measured by virtual LVDT) and crack width distribution of HTPP-ECC along the center line at AOI (from images captured at 8 individual strain values)

parallel to the loading axis by using the DIC data. For example the strain distribution peaks of image L_0134 (at 3.13% tensile strain measured by virtual LVDT), along the center axis parallel to loading direction is plotted in Fig. 6 (top). Positive strain peaks were used in crack width

calculations since negative peaks were caused by computational errors or from special subsets adjacent to a crack experiencing relative contraction (Ohno and Li 2014). Crack widths were computed from the ϵ_{xx} strain map by integrating strain with respect to length over the strain peak. However, even in uncracked regions, some fluctuation in the strain distribution because of the surface roughness heterogeneity of specimen was observed. Therefore, small individual peaks where there was no strain contour in corresponding DIC map locations were not counted as a crack. In most cases peaks less than 0.5% local strain have been neglected. On the other hand, an extensively widened single crack in reality can be accounted as two or three closely spaced cracks by the proposed integration methodology. In that case, the cumulative sum of these widths values was accepted as a single crack width since they arised due to the strain contour variation of a single crack in reality.

Due to the above mentioned reasons, the number of cracks and their location were manually checked by using strain maps and the crack numbers obtained by the proposed methodology are modified (Fig. 6). The resolution of images was 21 μm per pixel and the step of sampling points for strain calculation was 3. Crack analysis results and their corresponding strain values from LVDTs for each analyzed image have been listed in Table 2. It is important to note that crack widths at the center line parallel to loading axis were determined. Due to this reason initially formed cracks at the right side of the specimen were not detected before they reach to the center line (images L_0020 and L_0025) (Fig. 5). The initiation and development of each crack width intersecting the center line can be monitored from Fig. 6 (bottom). This graph permits to follow the variation of a crack width as a function of time at any specific location. In some cases, crack width decrease compared to previous value can be observed. This situation can be attributed to the stress level decrease due to the formation of new cracks and/or unstable widening of a previously formed crack which has reached its fiber bridging capacity. Stress level fluctuations may also provide elastic recovery of stretched fibers bridging the cracked section surfaces which temporary decreased the crack width.

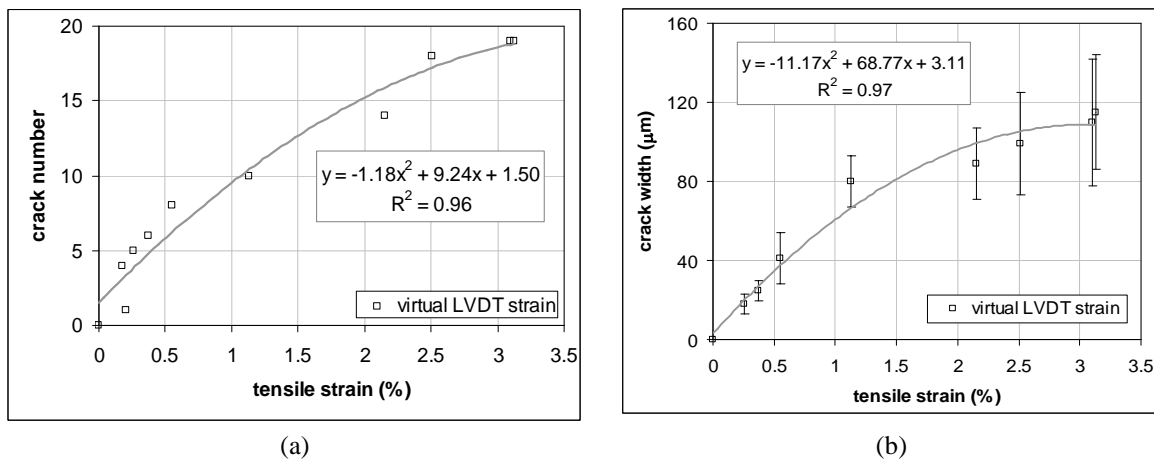


Fig. 7 Crack number (a) and crack width development (b) of HTPP-ECC specimen determined by virtual LVDTs at center x-x axis line (Fig. 6) with increasing tensile strain. (Note: Vertical bars at Fig. 7 indicate ± 1 standard deviation of crack width. The averages of three virtual LVDTs were used in the calculation of standard deviations)

The development of crack number and crack width calculated by using virtual LVDT strain values have been plotted in Fig. 7(a) and 7(b) respectively. These figures confirmed that it is possible to quantify the number of cracks formed and crack width at any specific strain value by using the crack determination method proposed in this study. Results permitted to characterize the multiple cracking potential of HTPP-ECC; 19 cracks formed before the exhaust of fiber bridging potential at the weakest section in terms of fiber dosage and orientation. The average crack width first suddenly increased up to 80 μm before 1% tensile strain with only 8 cracks. Then the crack widening rate decreased and crack widths nearly stabilized between 80-150 μm thanks to the formation of additional 11 new cracks. Formation of these new cracks and conservation of crack bridging potential of fibers at previously formed cracks promoted the tensile ductility of HTPP-ECC up to ~3-3.5% strain.

The size and amount of cracks formed at repeatedly captured images can also be monitored from crack width histograms determined by the proposed DIC based methodology (Fig. 8). Most the crack widths were less than 50 μm at initial periods of testing (L_0030-L_0040) and the major portion of cracks fell into the 26-50 μm range. In addition to increase in the number of cracks, initially left-skewed crack size distribution tended to skew right with increasing crack widths. Nearly 80% of the cracks were in the size range of 76-150 μm at about 3% strain. Major crack extended at the end of testing which was the main cause of specimen failure. In this case major crack formed out of AOI and it was not counted in crack analysis.

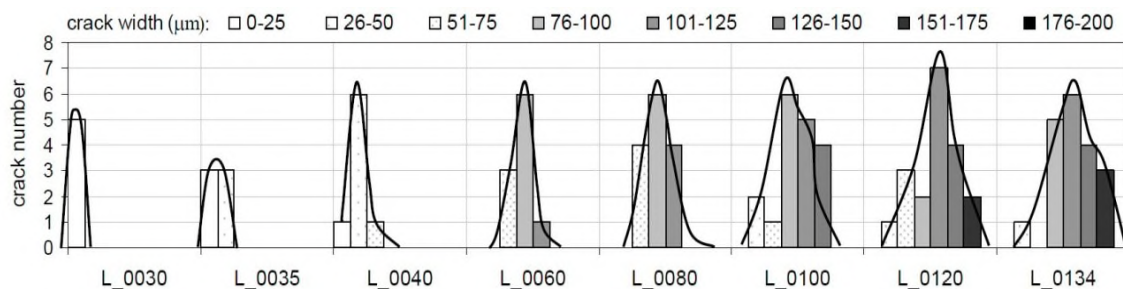


Fig. 8 Crack width histograms of each image captured at selected strain values (see Fig. 5 and Table 2 for image codes)

Determination of crack width distribution of cement based materials is of vital importance in terms of durability, since it has a direct influence on water permeability. When the crack opening displacement increases from 50 μm to about 200 μm , concrete permeability increases rapidly (Wang *et al.* 2007). From this point, ECC may bring significant durability advantages compared to conventional concrete and/or fiber reinforced concrete exhibiting single cracking (Şahmaran and Li 2009). The characteristic crack width distribution of ECC under loading also determines its self healing performance (Ranade *et al.* 2014). Previous studies showed that ECCs exhibiting tight and saturated multiple cracking at a given strain is more durable and present better self-healing behavior compared to the ones presenting comparatively wider cracks (Şahmaran *et al.* 2013). A critical threshold of 100 μm crack width measured at unloaded situation is usually proposed for a fully recoverable crack with self-healing (Li and Herbert 2012). This is understandable since small crack width means less volume which is easier to heal with hydration and carbonation products

near the cracked surface (hydrated lime as carbonation product source and unhydrated cement). Furthermore, fibers at any cracked section with a tight opening still maintain their bridging potential that is needed to invoke smaller flaws at other sections of the HTPP-ECC. Multiple cracking potential at higher stress levels can be improved by this way. From this point, HTPP-ECC with 76-150 μm crack width interval at about 3% tensile strain is a potential candidate of highly durable and easily self-healing composite in addition to its superior ductility behavior. Further experimental research is needed to check the durability potential of HTPP-ECC.

4. Conclusions

Multiple cracking characterization of a HTPP-ECC specimen exhibiting 4.1 MPa tensile strength and 3.1% tensile ductility is performed. 134 images with 5 sec interval captured from the surface of specimen under tensile loading. Speckle pattern of these images have been analyzed by DIC method and 11 representative strain maps have been presented. The advantages of the concept of virtual LVDT have been discussed and comparisons performed against real LVDT. Crack number and crack width distributions were determined with a proposed methodology based on the strain map analysis. The following conclusions can be drawn:

1. Both real and virtual LVDTs presented similar strain values between 0.2-3%. At lower strain values difference between real and virtual LVDTs can be attributed to the initial deviation of specimen from the loading axis. Crack widening out of AOI was responsible for strain difference at the end of testing. Virtual LVDTs were found more sensitive to detect local surface strain variations at the initial and final periods of loading while real LVDTs were only capable of measuring the average displacement of the entire mass of specimen during testing.

2. The use of the DIC technique provided quantitative data on the amount and location of local ϵ_{xx} strain and more importantly local strain concentrations that can be related with cracking for HTPP-ECCs. Strain maps derived from DIC method permitted to accurately follow the initiation and propagation of any single crack at any specific location which was not possible with conventional displacement measurement techniques.

3. Time dependent distribution of damage and saturation of micro-cracking was monitored at a comparatively wide area (84.3 \times 27.6 mm) with a micrometer-scale resolution (21 μm per pixel). It was not possible to capture a single image of such a wide area by using any conventional microscope at the same resolution.

4. Multiple cracking potential of HTPP-ECC was demonstrated with the help of strain maps derived from DIC software. The average crack width first increased up to 80 μm before 1% tensile strain and then the crack widening rate decreased and crack widths nearly stabilized between 80-150 μm . Formation of new cracks and conservation of bridging potential of fibers at previously formed cracks improved the tensile ductility of HTPP-ECC up to ~3-3.5% strain.

5. The size and amount of cracks formed at repeatedly captured images have been determined from the crack width histograms. Initially left-skewed crack size distribution tended to skew right with increasing crack widths. Proposed methodology based on DIC can be used to evaluate the durability and self healing potential of HTPP-ECCs.

6. DIC based crack analysis method can also be used as a promising and versatile tool for quality control of ECC and other strain hardening cementitious composites developed in recent years. However, the determination of exact crack number and crack widths still needs some additional post-processing and further studies are needed to reduce the amount of computational

efforts which is mandatory for the practical success of this methodology.

Acknowledgements

The first author would like to thank Prof. V.C. Li, Director of Advanced Civil Engineering - Materials Research Laboratory (ACE-MRL: <http://ace-mrl.engin.umich.edu/>), University of Michigan, Ann Arbor, MI for the use of tensile testing and DIC setup in the preparation of this article. Authors are also thankful to Assoc.Prof.Dr. K.Tosun Felekoğlu, Assist.Prof.Dr. R.Ranade and M.Ohno for their helpful discussions on HTPP-ECC design and DIC methodology. Materials supply from Lafarge (cement), Headwaters (fly ash), WR Grace (HRWRA), and Saint-Gobain Brasil (HTPP fiber) is also gratefully acknowledged. The second author wishes to thank TUBITAK (The Scientific and Technological Research Council of Turkey) for scholarship support under Grant no:115R012 which made it possible for him to undertake this study.

References

- Abanto-Bueno, J. and Lambros, J. (2002), "Investigation of crack growth in functionally graded materials using digital image correlation", *Eng. Fract. Mech.*, **69**(14-16), 1695-1711.
- Aggelis, D.G., Verbruggen, S., Tsangouri, E., Tysmans, T. and Van Hemelrijck, D. (2016), "Monitoring the failure mechanisms of a reinforced concrete beam strengthened by textile reinforced cement using acoustic emission and digital image correlation", *Int. J. Smart Struct. Syst.*, **17**(1), 91-105.
- Bergonnier, S., Hild, F. and Roux, S. (2005), "Digital image correlation used for mechanical tests on crimped glass wool samples", *J. Strain Anal. Eng. De.*, **40**(2), 185-197.
- Caduff, D. and Van Mier, J.G.M. (2010), "Analysis of compressive fracture of three different concretes by means of 3D-digital image correlation and vacuum impregnation", *Cement Concrete Compos.*, **32**(4), 281-290.
- Canadinc, D., Efstathiou, C. and Sehitoglu, H. (2008). "On the negative strain rate sensitivity of Hadfield steel", *Scripta Mater.*, **59**(10), 1103-1106.
- Canal, L.P., Gonzalez, C., Molina-Aldareguia, J.M., Segurado, J. and Lorca, J. (2012), "Application of digital image correlation at the microscale in fiber-reinforced composites", *Compos.: Part A*, **43**(10), 1630-1638.
- Chakinala, S. (2013), "A study of algorithms based on digital image correlation for embedding in a full-field displacement sensor with subpixel resolution", M.Sc. Dissertation, The University of Akron, Ohio, USA, 134p.
- Chu, C., Ranson, W.F., Sutton, M.A. and Peters, W.H. (1985), "Applications of digital-image correlation techniques to experimental mechanics", *Experimental Mech.*, **25**(3), 232-244.
- Cintrón, R. and Saouma, V. (2008), "Strain measurements with the digital image correlation system vic-2D", Center for Fast Hybrid Testing Report, Department of Civil, Environmental and Architectural Engineering, University of Colorado, USA, Sept., 23p.
- Cofaru, C., Philips, W. and Paeppegem, W.V. (2010), "Improved Newton-Raphson digital image correlation method for full-field displacement and strain calculation", *Appl. Opt.*, **49**(33), 6472-6484.
- Dehnavi, M.Y., Khaleghian, S., Emami, A., Tehrani, M. and Soltani, N. (2014), "Utilizing digital image correlation to determine stress intensity factors", *Polym. Test.*, **37**, 28-35.
- Dilibal, S. (2013), "Investigation of nucleation and growth of detwinning mechanism in martensitic single crystal NiTi using digital image correlation", *Metallogr. Microstruct. Anal.*, **2**(4), 242-248.
- Efstathiou, C. and Sehitoglu, H. (2010). "Strain hardening and heterogeneous deformation during twinning in Hadfield steel", *Acta Mater.*, **58**(5), 1479-1488.

- Felekoğlu, B., Tosun-Felekoğlu, K., Ranade, R., Zhang, Q. and Li, V.C. (2014), "Influence of matrix flowability, fiber mixing procedure, and curing conditions on the mechanical performance of HTPP-ECC", *Compos., Part B: Eng.*, **60**, 359-370.
- Gencturk, B., Hossain, K., Kapadia, A., Labib E. and Mo, Y.L. (2014), "Use of digital image correlation technique in full-scale testing of prestressed concrete structures", *Measurement*, **47**, 505-515.
- Ghorbani, R., Matta, F. and Sutton, M.A. (2015), "Full-field deformation measurement and crack mapping on confined masonry walls using digital image correlation", *Experimental Mech.*, **55**(1), 227-243.
- Godara, A. and Raabe, D. (2007). "Influence of fiber orientation on global mechanical behavior and mesoscale strain localization in a short glass-fiber-reinforced epoxy polymer composite during tensile deformation investigated using digital image correlation", *Compos. Sci. Tech.*, **67**(11-12), 2417-2427.
- Hild, F., Raka, B., Baudequin, M., Roux, S. and Cantelaube, F. (2002), "Multiscale displacement field measurements of compressed mineral-wool samples by digital image correlation", *Appl. Opt.*, **41**(32), 6815-28.
- Hild, F. and Roux, S. (2006), "Measuring stress intensity factors with a camera: Integrated digital image correlation (I-DIC)", *C. R. Mecanique*, **334**(1), 8-12.
- Ikai, S., Reichert, J.R., Vasconcellos, A.R. and Zampieri, V.A. (2006), "Asbestos-free technology with new high tenacity PP-Polypropylene fibers in air-cured hatschek process", *Proceedings of the 10th. Int. Inorganic-Bonded Fiber Composites Conference (IIBCC)*, Universidade de Sao Paulo & University of Idaho: Sao Paulo, Brazil, 33-48.
- Jerabek, M., Major, Z. and Lang, R.W. (2010), "Strain determination of polymeric materials using digital image correlation", *Polym. Test.*, **29**(3), 407-416.
- JSCE (2008), "Recommendations for design and construction of high performance fiber reinforced cement composites with multiple fine cracks (HPFRCC)", *Concrete Committee*, Rokugo K. (chair), Japan Society of Civil Engineers, March, 212.
- Kashfuddoja, M., Prasath, R.G.R. and Ramji, M. (2014), "Study on experimental characterization of carbon fiber reinforced polymer panel using digital image correlation: A sensitivity analysis", *Opt. Laser Eng.*, **62**, 17-30.
- Leplay, P., Réthoré, J., Meille, S. and Baietto, M.C. (2010), "Damage law identification of a quasi brittle ceramic from a bending test using digital image correlation", *J. Eur. Ceramic Society*, **30**(13), 2715-2725.
- Li, V.C. and Herbert, E.N. (2012), "Robust self-healing concrete for sustainable infrastructure", *J. Adv. Concrete Tech.*, **10**(6), 207-218.
- Li, V.C. (2012), "Tailoring ECC for special attributes: a review", *Int. J. Concrete Struct. Mater.*, **6**(3), 135-144.
- Li, V.C., Wang, S. and Wu, C. (2001), "Tensile strain-hardening behavior of PVA-ECC", *ACI Mater. J.*, **98**(6), 483-492.
- Lin, Z., Kanda, T. and Li, V.C. (1999), "On interface property characterization and performance of fiber reinforced cementitious composites", *J. Concrete Sci. Eng.*, **1**, 173-184.
- Liu, Y., Cho, S., Spencer, B.F. and Fan J. (2014), "Automated assessment of cracks on concrete surfaces using adaptive digital image processing", *Int. J. Smart Struct. Syst.*, **14**(4), 719-741.
- Malesa, M., Malowany, K., Tomczak, U., Siwek, B., Kujawinska, M. and Sieminska-Lewandowska, A. (2013), "Application of 3D digital image correlation in maintenance and process control in industry", *Comput. Ind.*, **64**(9), 1301-1315.
- Ohno, M. and Li, V.C. (2014), "A feasibility study of strain hardening fiber reinforced fly ash-based geopolymer composites", *Constr. Build. Mater.*, **57**, 163-168.
- Pan, B., Wu, D. and Xia, Y. (2012). "An active imaging digital image correlation method for deformation measurement insensitive to ambient light", *Opt. Laser Tech.*, **44**(1), 204-209.
- Pan, B., Xie, H., Wang, Z., Qian, K. and Wang, Z. (2008), "Study on subset size selection in digital image correlation for speckle patterns", *Opt. Society America, Opt. Express*, **16**(10), 7037-7048.
- Passieux, J.C. and Perie, J.N. (2012), "High resolution digital image correlation using proper generalized decomposition: PGD-DIC", *Int. J. Numer. Method. Eng.*, **92**(6), 531-550.

- Ranade, R., Zhang, J., Lynch, J.P. and Li, V.C. (2014), "Influence of micro-cracking on the composite resistivity of Engineered Cementitious Composites", *Cement Concrete Res.*, **58**, 1-12.
- Roux, S., Rethore, J. and Hild, F. (2009), "Digital image correlation and fracture: an advanced technique for estimating stress intensity factors of 2D and 3D cracks", *J. Phys. D: Appl. Phys.*, **42**, 1-21.
- Shah, S.G. and Kishen, J.M.C. (2011), "Fracture properties of concrete-concrete interfaces using digital image correlation", *Experimental Mech.*, **51**(3), 303-313.
- Shih, M.H. and Sung, W.P. (2013), "Application of digital image correlation method for analysing crack variation of reinforced concrete beams", *Sadhana*, **38**(4), 723-741.
- Sutton, M.A., Orteu, J.J. and Schreier, H. (2009), *Image Correlation for Shape, Motion and Deformation Measurements. Basic Concepts, Theory and Applications*, Springer, Verlag, USA.
- Sutton, M.A., Wolters, W.J., Peters, W.H., Ranson, W.F. and McNeill, S.R. (1983), "Determination of displacements using an improved digital correlation method", *Image Vision Comput.*, **1**(3), 133-139.
- Sutton, M.A., Yan, J.H., Tiwari, V., Schreier, H.W. and Orteu, J.J. (2008), "The effect of out-of-plane motion on 2D and 3D digital image correlation measurements", *Opt. Laser. Eng.*, **46**(10), 746-757.
- Şahmaran M. and Li, V.C. (2009). "Durability properties of micro-cracked ECC containing high volumes fly ash", *Cement Concrete Res.*, **39**(11), 1033-1043.
- Şahmaran, M., Yıldırım, G. and Erdem, T.K. (2013), "Self-healing capability of cementitious composites incorporating different supplementary cementitious materials", *Cement Concrete Compos.*, **35**(1), 89-101.
- Tao, G. and Xia, Z. (2005), "A non-contact real-time strain measurement and control system for multiaxial cyclic/fatigue tests of polymer materials by digital image correlation method", *Polym. Test.*, **24**(7), 844-855.
- Tung, S.H., Shih, M.H. and Sung, W.P. (2008), "Development of digital image correlation method to analyse crack variations of masonry wall", *Sadhana*, **33**(6), 767-779.
- Tung, S.H. and Sui, C.H. (2010), "Application of digital-image-correlation techniques in analysing cracked cylindrical pipes", *Sadhana*, **35**(5), 557-567.
- Wang, K., Jansen, D.C., Shah, S.P. and Karr, A.F. (2007), "Permeability study of cracked concrete", *Cement Concrete Res.*, **27**(3), 381-393.
- Wang, Y. and Cuitino, A.M. (2002), "Full-field measurements of heterogeneous deformation patterns on polymeric foams using digital image correlation", *Int. J. Solid. Struct.*, **39**(13-14), 3777-3796.
- Willems, A., Lomov, S.V., Verpoest, I. and Vandepitte, D. (2009), "Drape-ability characterization of textile composite reinforcements using digital image correlation", *Opt. Laser. Eng.*, **47**(3-4), 343-351.
- Wu, Z.M., Rong, H., Zheng, J.J., Xu, F. and Dong, W. (2011), "An experimental investigation on the FPZ properties in concrete using digital image correlation technique", *Eng. Fract. Mech.*, **78**(17), 2978-2990.
- Yang, E.H. (2007), "Designing added functions in engineered cementitious composites", Ph.D. Dissertation, The University of Michigan, USA, 276p.
- Yaofeng, S. and Pang, J.H.L. (2007), "Study of optimal subset size in digital image correlation of speckle pattern images", *Opt. Laser. Eng.*, **45**(9), 967-974.